

# Infrared and Raman studies of hydroxide ions in NaCl extended to H → D and $^{16}\text{O} \rightarrow ^{18}\text{O}$ isotope exchange

E. Gustin, A. Bouwen, and D. Schoemaker

*Physics Department, University of Antwerp (U.I.A.), Universiteitsplein 1, B-2610 Antwerpen, Belgium*

C. P. An and F. Luty

*Physics Department, University of Utah, Salt Lake City, Utah 84112*

(Received 28 September 2000; published 26 February 2001)

Substitutional  $\text{OH}^-$  and  $\text{OD}^-$  defects in NaCl have been studied with Fourier-transform infrared (FTIR) and polarized Raman-scattering (RS) spectroscopy. For the first time, the motional levels of the  $\text{OH}^-$  were clearly resolved in their stretch-mode (SM) absorption spectra, showing no change in splitting under  $^{16}\text{OH}^- \rightarrow ^{18}\text{OH}^-$  isotope exchange. Due to extremely small oscillator strengths, the first harmonic SM absorptions of  $^{16}\text{OD}^-$  and  $^{18}\text{OD}^-$  defects were not detectable. In contrast to this, the almost equal RS strengths of  $\text{OH}^-$  and  $\text{OD}^-$  defects permitted their detailed comparative investigation with polarized Raman scattering. The resulting low-frequency motional levels of  $\text{OD}^-$  in both ground and excited SM states are found to be quite different from those of  $\text{OH}^-$  and are hard to reconcile with some of the existing models. A reasonably good fit of the  $\text{OH}^-$  and  $\text{OD}^-$  data can be achieved with a simple  $V_4$  Devonshire model; this suggests hindered rotation of a strongly off-center shifted center of mass in a potential with smaller energy barriers for  $\text{OD}^-$  compared to  $\text{OH}^-$ . Despite the unexplained weakness of the first harmonic SM absorption of  $\text{OD}^-$ , phonon and librational sidebands are observed with almost similar strength as those of  $\text{OH}^-$ . Their symmetry was determined by polarized RS and/or FTIR absorption measurements under uniaxial stress alignment. The “normal”  $\text{OH}^-/\text{OD}^-$  isotope shift of the librational sideband and the observation of its second harmonic show that this angular motion occurs around the center of mass in a strong and nearly harmonic potential.

DOI: 10.1103/PhysRevB.63.134301

PACS number(s): 61.72.Ji, 66.35.+a, 71.55.-i

## I. INTRODUCTION

For the understanding of the reorientational tunneling of  $\text{OH}^-$  ions observed in many ionic solids and glasses, dilute substitutional  $\text{OH}^-$  defects in alkali-halide crystals have served as simple and well-defined model systems. By Coulomb and short-range repulsive interactions with the surrounding lattice, the egg-shaped  $\text{OH}^-$  molecules form an effective reorientational potential, the equivalent minima of which determine for each host their molecular orientations.

Since the beginning of this field about 35 years ago, the most abundant studies have been for  $\text{OH}^-$  in crystals built from  $\text{Na}^+$ ,  $\text{K}^+$ ,  $\text{Rb}^+$  cations and  $\text{Cl}^-$ ,  $\text{Br}^-$ ,  $\text{I}^-$  anions. These yielded  $\langle 100 \rangle$  orientations for all cases except one, (the  $\langle 110 \rangle$ -oriented  $\text{KI}:\text{OH}^-$ ).<sup>1</sup> In spite of this apparent simplicity, these systems are much more complicated compared to the expectations of the initial theoretical models:<sup>2</sup> due to the shape and size (like an elongated  $\text{F}^-$  ion) of  $\text{OH}^-$ , its substitution into the much larger anion vacancies of these hosts can lead to sizable off-center shifts of its center of mass (c.m.) and center of charge. Moreover, gerade and ungerade distortions of the surrounding cubic lattice will add an extra “dressing effect” to the bare molecule in each  $\langle 100 \rangle$  orientation.<sup>3,4</sup> The resulting electric-dipole vector and elastic-dipole tensor contain a combination of these molecular, displacement, and dressing properties. Their static  $\langle 100 \rangle$  symmetry, and the “cigar-shape” of the elastic tensor have been mostly determined by dichroism measurements of either the electronic (ultraviolet, UV) or vibrational (infrared, IR) absorption of  $\text{OH}^-$ , aligned under applied electrical

fields or stress.<sup>5,6</sup> Time-dependent electro-optical or electrocaloric measurements revealed the  $\text{OH}^-$  reorientation kinetics as a one-phonon-assisted tunneling process with a linearly  $T$ -dependent rate.<sup>7</sup> The observed strong decrease of this rate for hosts with growing cation mass and lattice parameters<sup>8</sup> was attributed to an increase of the dressing effect that hinders reorientational tunneling. For this group of crystals, the smallest hindering effect and largest tunneling splitting of  $\text{OH}^-$  was found in NaCl.

Beyond this endpoint of the hosts with  $\langle 100 \rangle$  oriented  $\text{OH}^-$  impurities lie only the alkali fluorides. In this new group, reorientational tunneling of  $\text{OH}^-$  has been doubted for a long time due to its very tight fit into the small  $\text{F}^-$  vacancy. Only our very recent stress-optical FTIR<sup>9</sup> and polarized Raman<sup>10</sup> studies in LiF, NaF, and KF have revealed the  $\text{OH}^-$  reorientational properties, which are simpler and very much in contrast to the ones in the above-discussed group of hosts. The molecules have  $\langle 111 \rangle$  oriented disk-shaped elastic-dipole tensors and small electric-dipole moments, without substantial c.m. off-center shifts or dressing effects. This latter was confirmed by systematic  $\text{OH}^- \rightarrow \text{OD}^-$  isotope exchange experiments,<sup>9,10</sup> which showed by the resulting strong reduction of tunneling splitting  $\Delta$  that in these hosts the H or D atom is essentially the reorienting particle. For the hosts with  $\langle 100 \rangle$  oriented  $\text{OH}^-$  ions, a very different isotope effect can be expected: due to sizable off-center and dressing properties, translational, and rotational motion of both H and O should play a role in reorientational tunneling. By far the most interesting and attractive system to study this is the  $\langle 100 \rangle$  borderline system  $\text{NaCl}:\text{OH}^-$  with

its large well-resolvable tunneling splitting  $\Delta$ . In spite of extensive earlier studies of this system (which we will review in Sec. III A), the question of isotope exchange effects on reorientational tunneling has essentially not yet been addressed or solved. We try to do this in this paper with FTIR absorption and Raman-scattering spectroscopy, employing both  $H \rightarrow D$  and  $^{16}O \rightarrow ^{18}O$  isotope exchange.

## II. EXPERIMENTAL DETAILS

The crystals were grown at the University of Utah, with the Kyropoulos technique from a melt of ultrapure powder doped with a proper sodium hydroxide. The “normal” doping-material  $Na^{16}OH$  was also used to synthesize by reaction with water isotopes  $H_2^{18}O$ ,  $D_2^{16}O$ , and  $D_2^{18}O$  the isotopic doping materials  $Na^{18}OH$ ,  $Na^{16}OD$ , and  $Na^{18}OD$ , respectively. For the growth of  $OD^-$ -doped crystals, the normally used Ar atmosphere was mixed with about 30% of  $D_2$  gas to avoid back conversion of  $OD^-$  to unwanted  $OH^-$ . The concentration of  $OH^-$  was determined to within an accuracy of 10% by  $pH$  analysis, the intensity of the near-infrared stretch mode and the intensity of the UV electronic absorption. For  $OD^-$ -doped samples, the SM infrared absorption of isolated defects is not detectable. Therefore, the total concentration was determined by  $pH$  analysis and electronic UV absorption instead, and the  $OH^-$  concentration was subtracted. We assumed the UV oscillator strength to be identical for  $OH^-$  and  $OD^-$ .<sup>11</sup> This procedure is less accurate, and results in an uncertainty of about 25%.

The IR absorption spectra were measured with a Bruker IFS88 FTIR spectrometer with a resolution of  $\geq 0.1 \text{ cm}^{-1}$ . The Raman-scattering experiments were performed with a Dilor XY-800 Raman Spectrometer, equipped with a Wright Instruments nitrogen-cooled  $1200 \times 300$ -pixel CCD detector. The 514.53 nm line of a Spectra Physics 2020  $Ar^+$  laser was used as excitation source. Due to the weakness of the Raman signal, fairly high-excitation powers between 700 and 1400 mW were used. This resulted in considerable local heating. The temperature at the focus point was calculated from the intensity ratio of Stokes and anti-Stokes low-frequency spectra, and was found to be about 5 K higher than the heat-exchanger temperature. Spectral resolution was  $1.7\text{--}1.5 \text{ cm}^{-1}$  in the low-dispersion mode of the spectrometer, and of  $0.3 \text{ cm}^{-1}$  in the high-dispersion mode. Depending on the strength of the elastic scattering, we can measure the Raman spectrum down to between 5 and  $10 \text{ cm}^{-1}$ , but it is hard to determine this lower limit accurately because the filtering of the spectrum in this spectrometer mode does not have an ideally sharp edge. This distorts the spectrum in the lowest few wave numbers.

All Raman-scattering experiments were performed in a  $90^\circ$  scattering geometry. Samples cleaved along (100) surfaces were used to record  $\langle 100,100 \rangle$  (or  $A_{1g} + E_g$ ) and  $\langle 100,010 \rangle$  ( $\frac{1}{2}T_{2g}$ ) spectra. Samples polished to have two (110) surfaces gave us  $\langle 110,1\bar{1}0 \rangle$  ( $\frac{3}{4}E_g$ ) and  $\langle 110,110 \rangle$  ( $A_g + \frac{1}{4}E_g + \frac{1}{2}T_{2g}$ ) spectra. Note that for the symmetry notations  $E_g$  and  $T_{2g}$ , we are using the convention of Ref. 12, which differs from the one used by Ref. 13 by factors  $4/3$  and  $2$ , respectively.

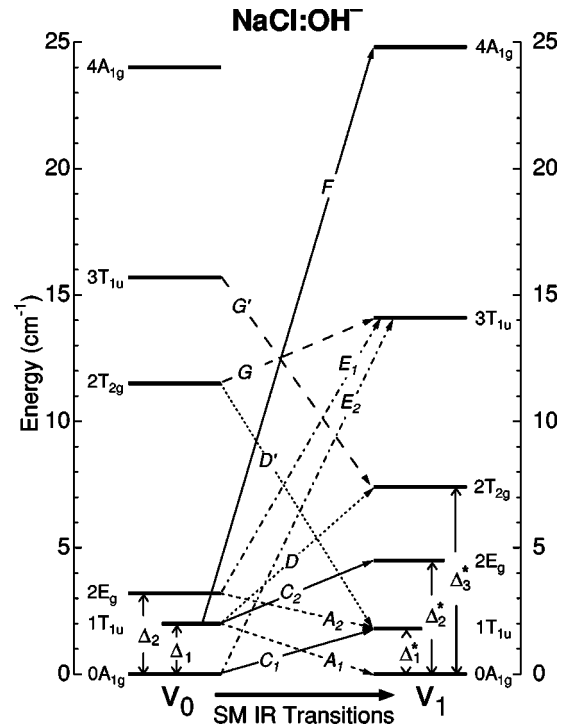


FIG. 1. Low-energy levels of  $OH^-$  in its ground ( $v_0$ ) and excited ( $v_1$ ) SM state. The diagram is based on the indicated FTIR transitions, observed in Fig. 2. The  $3T_{2u}$  levels, expected somewhere between  $3T_{1u}$  and  $4A_{1g}$ , have not been determined. This level diagram is in very good agreement with the one derived from the  $v_0 \rightarrow v_1$  transitions by Peascoe and Klein (Ref. 13).

## III. MOTIONAL STATES OF $OH^-$ IN NaCl

### A. Review of previous work

Before we describe our experiments on the  $OH^-$  impurity, we give a brief review of some earlier published studies, to provide the context for the interpretation of our own results. It is crucial to understand that some experimental techniques probe only the states in the vibrational ground state, while all studies of SM transitions involve combinations of energy levels in the ground state ( $v_0$ ) and levels in the first excited state ( $v_1$ ) of the SM vibration. Figure 1 shows an energy level diagram, based in part, on our measured IR transitions, which are indicated in the figure, and in part, on published data as discussed below. It is evident that the energy levels in the states  $v_0$  and  $v_1$  are significantly different. Also, because numerous nonequidistant levels have been identified, the splitting cannot be described with a single parameter. As shown in Fig. 1, we use in the case of  $v_0$ , the notation  $\Delta_1$  (or  $\Delta_2$ ) for the splitting between the lowest and first (or second) tunneling state; similarly in case of  $v_1$ , the notations  $\Delta_1^*$ ,  $\Delta_2^*$ , and  $\Delta_3^*$  are used for the splittings from the lowest level up to the first, second and third level, respectively.

Kirby *et al.*<sup>14</sup> studied the  $v_0 \rightarrow v_0$  transitions with a far-infrared absorption technique, and found a complicated spectrum in the range  $0\text{--}25 \text{ cm}^{-1}$ . With the potential barrier of the rotational motion estimated from the measured librational frequency, they concluded that the sizable reorientational

tunneling of the molecular axis could account for the lowest three levels. To explain these higher transitions above the tunneling levels, they adopted a model that also included translational motions of the c.m. around its  $\langle 100 \rangle$  equilibrium position, parallel and perpendicular to its off-center shift. The two excited states of this translational motion are also split by reorientational tunneling motion, creating a complicated set of energy levels. The values for  $\Delta_1$  and  $\Delta_2$  derived from this model were 2 and  $3 \text{ cm}^{-1}$ .

The scattering of phonons by the levels in the ground state has been investigated with much lower spectral resolution by thermal conductivity measurements.<sup>15</sup> These revealed the presence of more than one tunneling level in the  $0.9$  to  $2.8 \text{ cm}^{-1}$  region. The experimental curve could be fitted reasonably well to an energy level diagram based mostly on the far-infrared absorption data, using splittings of  $\Delta_1 = 1.9 \text{ cm}^{-1}$  and  $\Delta_2 = 2.8 \text{ cm}^{-1}$ , and higher levels present up to  $22 \text{ cm}^{-1}$ .

Later, Windheim and Kinder determined the splitting  $\Delta_2 = 3.3 \text{ cm}^{-1}$  with phonon spectroscopy.<sup>16</sup> Their results under applied  $\langle 100 \rangle$  uniaxial stress fit very well to a model of  $\langle 100 \rangle$  dipoles, with an elastic-dipole moment  $\alpha = 6.09 \times 10^{24} \text{ cm}^3$ . However, this does not necessarily mean that the molecule has a  $\langle 100 \rangle$  orientation, because the elastic-dipole tensor might also represent the off-center shift of the molecule with a different orientation.

A study of the electrochromism of the UV electronic absorption band of the  $\text{OH}^-$  revealed a dichroism that is compatible with a  $\langle 100 \rangle$  orientation, but not with  $\langle 111 \rangle$  and  $\langle 110 \rangle$  orientations.<sup>5</sup> It is also very similar to that observed in  $\text{RbCl}$  and  $\text{KBr}$  hosts, for which the  $\langle 100 \rangle$  orientation of the  $\text{OH}^-$  has been quite convincingly demonstrated.

Peascoe and Klein measured both low-frequency ( $\nu_0 \rightarrow \nu_0$ ) and high-frequency ( $\nu_0 \rightarrow \nu_1$ ) polarized Raman spectra.<sup>13</sup> In contrast to the prediction of the Kirby *et al.* model, no  $A_{1g}$  translational Raman transitions were observed in the low-frequency measurements. Therefore, it was concluded that the translational motion parallel to the off-center shift did not exist as a pure mode. A modified model was suggested with strongly coupled translation-reorientational tunneling: The motion of the c.m. between six  $\langle 100 \rangle$  off-center wells is followed adiabatically by reorienting the equilibrium direction of the molecular axis. This coupled motion was treated with a simple Devonshire potential<sup>17</sup> of a weakly hindered rotor or an off-center monatomic defect. The observed Raman transitions together with the earlier SM absorption data<sup>18</sup> could well be fitted to simple  $V_4$  Devonshire energy levels, yielding  $\Delta_1 = 2.0$  and  $\Delta_2 = 3.2 \text{ cm}^{-1}$  for  $\nu_0$ , and different  $\Delta_1^* = 1.8$  and  $\Delta_2^* = 4.5 \text{ cm}^{-1}$  values for  $\nu_1$ .

A later analysis of the polarized Raman spectra with the behavior type method<sup>19</sup> confirmed that the molecular orientation is close to  $\langle 100 \rangle$ , although allowing for the possibility that it slightly deviates from this.<sup>12</sup>

Suto and Ikezawa<sup>20</sup> determined  $\Delta_1 = 1.85 \text{ cm}^{-1}$  and  $\Delta_2 = 3.41 \text{ cm}^{-1}$  with millimeter wave absorption spectroscopy. To explain the energy-level structure, they made a linear combination of atomic orbitals-molecular-orbital (LCAO-MO) calculation in which the center of mass of the  $\text{OH}^-$

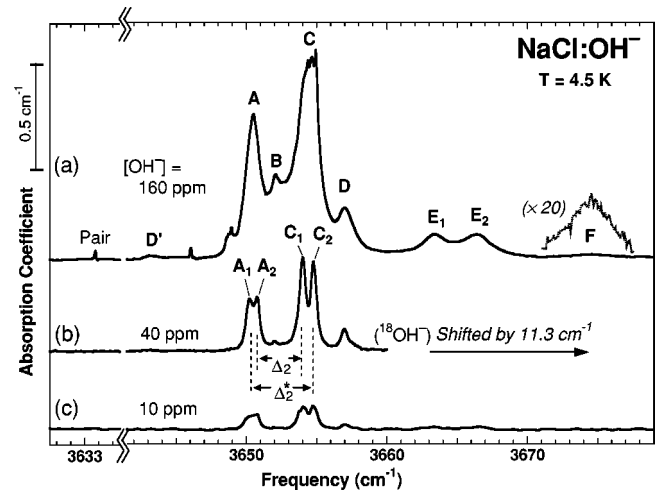


FIG. 2. FTIR spectra of the SM transitions between the low energy  $\nu_0$  and  $\nu_1$  levels, measured at 4.5 K for (a)  $\text{NaCl} + 160 \text{ ppm OH}^-$ , (b)  $\text{NaCl} + 40 \text{ ppm } ^{18}\text{OH}^-$  [shifted by  $+11.3 \text{ cm}^{-1}$  for comparison with (a) and (c)], (c)  $\text{NaCl} + 10 \text{ ppm OH}^-$ .

moves between six off-center positions with potential wells of elliptic shape. This model explains the positions of the observed  $\nu_0 \rightarrow \nu_0$  transitions well, including one that is not explained by the Devonshire model. The reorientation of the molecular axis is assumed to take place in fundamentally the same way as in the previous model, i.e., adiabatically coupled to the motion of the center of mass between the wells.

Evidently, the choice of model has some consequences for the labeling of the states. The symmetry of the states alone does not uniquely identify the levels. Peascoe and Klein<sup>13</sup> included the rotational quantum number  $L$  in their assignment of levels, because they treated the system as a hindered rotor. Suto and Ikezawa<sup>20</sup> instead denoted the state of the translational oscillator that plays a central role in their model. Because Peascoe and Klein's paper is, for our purposes, the source of most reference data, we will use its notation for the levels. This makes a comparison of our values with the tables of Ref. 13 easier. This is a practical decision entirely, and should not be interpreted as a preference for the model proposed in that work.

## B. Infrared and Raman Experiments

Wedding and Klein<sup>18</sup> identified eight peaks in the SM absorption spectra at various  $\text{OH}^-$  concentrations, but they did not yet identify these as fine structure due to tunneling states. Peascoe and Klein<sup>13</sup> showed how these SM transitions could be interpreted in the framework of the level model they derived for  $\nu_0$  and  $\nu_1$  from Raman measurements. However, not all tunneling transitions had been clearly resolved, and a more recent work by Nanba *et al.*<sup>21</sup> also failed to achieve this. We have performed high-quality FTIR measurements of the SM absorption, to resolve all its tunneling splitting.

Figure 2 shows the SM absorption spectra of samples at three different concentrations. It is important to note that spectrum (b) was measured in a sample with  $40 \text{ ppm } ^{18}\text{OH}^-$

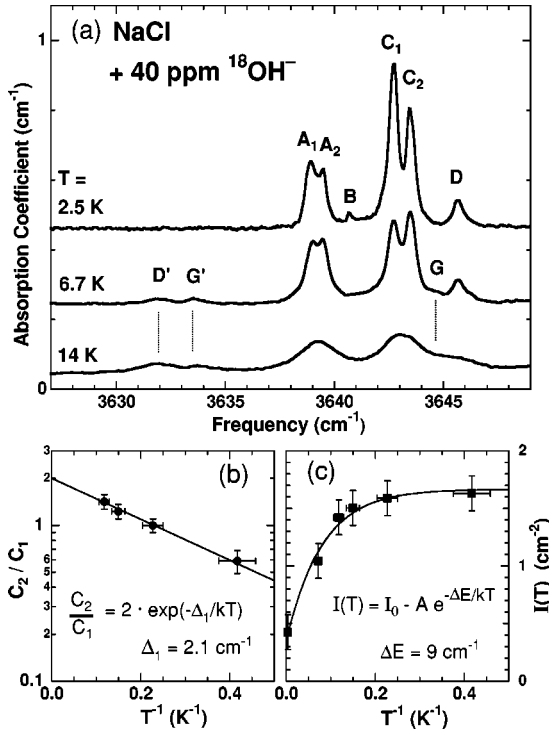


FIG. 3. (a) FTIR spectra of the SM transitions of  $^{18}\text{OH}^-$  in NaCl at three temperatures: 2.5, 6.7, and 14 K. (b) Ratio of the absorption strength  $C_1/C_2$  versus  $T^{-1}$ , yielding the activation energy  $\Delta_1$ . (c) Total SM absorption intensity, plotted linearly vs  $T^{-1}$ .

and was plotted in Fig. 2 after a shift of  $11.3\text{ cm}^{-1}$  (the expected isotope/reduced mass frequency change) to lower energy. Comparison of this shifted spectrum to that of the 10 ppm  $^{16}\text{OH}^-$  doped sample (c) shows that the spectral fine structure has not changed by the  $^{16}\text{O} \rightarrow ^{18}\text{O}$  isotope variation. In both cases of low concentration, the broad  $A$  and  $C$  bands from spectrum (a) each become resolved into two components. As due to its higher signal to noise ratio the spectral fine structure is better in the 40 ppm  $^{18}\text{OH}^-$  sample, we use it in Fig. 3(a) to show its temperature variation, plotted at its original (unshifted) frequency. At the lowest temperature ( $\approx 2.5\text{ K}$ ) the  $C_1$  band becomes dominant compared to the others, therefore it must be the  $0A_{1g} \rightarrow 1T_{1u}$  transition. Since the  $C_2$  band is the second dominant, it must be the transition from the first tunneling state  $1T_{1u}$  of  $\nu_0$  to  $2E_g$  of  $\nu_1$ . The absorption intensity ratio of  $C_2$  to the  $C_1$  as a function of temperature can be well-fitted to the Arrhenius relation [Fig. 3(b)], yielding the energy-level splitting  $\Delta_1$  to be  $2.1\text{ cm}^{-1}$ .

The components  $A_1$  and  $A_2$  are identified as the ‘‘anti-Stokes’’ transitions of  $C_1$  and  $C_2$ , respectively. Their accurately measured frequencies provide the lower level splitting parameters,  $\Delta_1^* = 1.7\text{ cm}^{-1}$ ,  $\Delta_2 = 3.2\text{ cm}^{-1}$ , and  $\Delta_2^* = 4.5\text{ cm}^{-1}$ . These parameters are in good agreement with the previous studies.

As concentration increases in Fig. 2, a new line  $B$  appears, growing faster than linearly with increasing concentration. It most probably represents the classical SM transition of  $\text{OH}^-$  oscillators for which the tunneling splitting is suppressed by

interactions between the molecules, other imperfections, or background strain. In Ref. 21, the  $B$  band was described to a pair line because of its stated quadratic concentration dependence. In our analysis, the intensity of the  $B$  line increases with a lower power ( $< 2$ ) of the concentration, which is hard to determine accurately due to the rising overlap with the  $A$  and  $C$  bands at higher concentrations. We found, in fact, a sharp line at  $3636.2\text{ cm}^{-1}$  (see left side of Fig. 2), which carries all features of a pair line: exact quadratic concentration dependence, much smaller width than all isolated  $\text{OH}^-$  absorptions, and appearance of splitting due to  $\text{OH}^-/\text{OD}^-$  mixed pairs in double-doped crystals.

At high concentration [see Fig. 2(a)], the other transitions, which involve the energy levels above  $2E_g$ , are observed. They too fit into the energy-level diagram of Fig. 1, with  $D$  assigned to the  $1T_{1u} \rightarrow 2T_{2g}$ , and  $E_1$  to the  $2E_g \rightarrow 3T_{1u}$  transition.  $E_2$  might very well be the  $0A_{1g} \rightarrow 3T_{1u}$  as indicated on Fig. 1, in agreement with the observed increase of the  $E_1/E_2$  ratio at higher temperature. The extremely weak  $F$  transition can be assigned to  $1T_{1u} \rightarrow 4A_{1g}$ .

Anti-Stokes-type IR transitions  $D'$  and  $G'$  are observed as temperature increases [see Figs. 2(a) and 3(a)].  $D'$  is assigned to the  $2T_{2g} \rightarrow 1T_{1u}$  transition, and  $G'$  to the  $3T_{1u} \rightarrow 2T_{2g}$ . The equivalent Stokes transition  $G$  is barely detectable between the  $C_2$  and  $D$  bands at 6.7 K in Fig. 3.

Besides the appearance of anti-Stokes absorptions, increase of temperature results in two effects: loss of the spectral fine structure (due to broadening of the individual lines), and loss of integrated SM absorption intensity. The latter effect is illustrated in Fig. 3(c) for  $^{18}\text{OH}^-$ , but is also observed similarly for  $^{16}\text{OH}^-$ . At room temperature, only 20% of the intensity at 2.5 K remains. As far as could be detected, this is not compensated by an absorption increase in the SM sidebands, discussed in Sec. VB. Such a strongly temperature-dependent SM absorption intensity has not been observed for  $\text{OH}^-$  in other alkali-halide hosts. The measured temperature dependence follows an exponential law with an activation energy of  $\approx 9\text{ cm}^{-1}$ , which corresponds approximately to the energy difference between the average of three lowest levels and the  $2T_{2g}$  state. This implies that the absorption intensity could be linked in some way to the thermal population of higher energy levels that give rise to smaller absorption. Such an effect could have some relation to the observed weakness of the  $\text{OD}^-$  absorption, described and discussed in Sec. IV A.

We also performed measurements at 5 K of the elastic dichroism of the SM absorption. For the 10 ppm  $\text{OH}^-$  crystal, our result under  $\langle 100 \rangle$  stress can be fitted reasonably well to a cigar-shaped elastic dipole moment of  $\alpha = +6.2 \times 10^{24}\text{ cm}^3$ , close to the value determined by phonon spectroscopy.<sup>16</sup>

We also performed several polarized Raman-scattering experiments on  $\text{OH}^-$ , mostly for direct comparison with  $\text{OD}^-$ ; some of these  $\text{OH}^-$  spectra will be shown in Sec. IV B. Both low- and high-frequency spectra are similar to the data of Ref. 13, and showed very little new details. As one minor extension, we observed at 10 K a shoulder of the

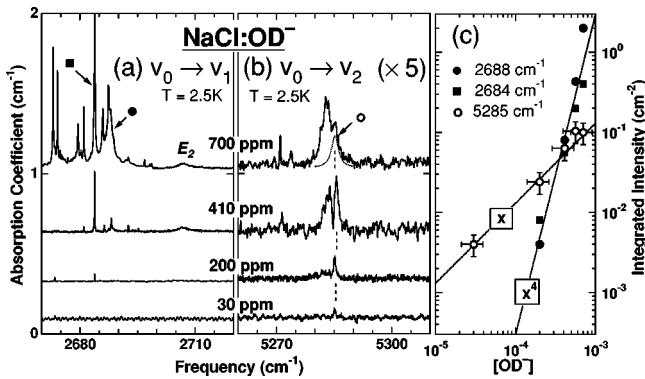


FIG. 4. SM absorption spectra of NaCl samples with four different  $\text{OD}^-$  concentrations, measured at 2.5 K in the first harmonic (a) and second harmonic (b) SM spectral range. In (c) the strength of three selected transitions [marked in (a) and (b) with identical symbols] is plotted in a double-logarithmic scale versus the concentration.

$0A_{1g} \rightarrow 0A_{1g}$  transition, about  $0.9 \text{ cm}^{-1}$  above the SM frequency. Most likely this is the  $2E_g \rightarrow 2E_g$  transition, which was expected to be found with a shift of  $1.3 \text{ cm}^{-1}$ .

#### IV. MOTIONAL STATES OF $\text{OD}^-$ IN NaCl

In comparison with the extensive previous literature on  $\text{OH}^-$  in NaCl, studies of the  $\text{OD}^-$  impurity have been very few, and mostly unsuccessful. Kirby *et al.* found no measurable  $v_0 \rightarrow v_0$  absorption that could be associated with the  $\text{OD}^-$ . The far-infrared spectrum of their  $\text{OD}^-$ -doped samples showed only the weak absorption of the small unwanted amount of  $\text{OH}^-$ .<sup>14</sup> Similarly, Wedding and Klein found no near-infrared SM ( $v_0 \rightarrow v_1$ )  $\text{OD}^-$  absorption, and concluded that its integrated absorption intensity must be at least 120 times smaller than that of  $\text{OH}^-$  for the same concentration.<sup>18</sup> At least partially successful was the study of thermal conductivity.<sup>15</sup> Its measured temperature variation was found to be very similar for  $\text{OH}^-$ - and  $\text{OD}^-$ -doped NaCl, indicating that the low-energy levels of both isotopes are of similar magnitude. In view of this lack of quantitative knowledge about the NaCl: $\text{OD}^-$  system, we study it in this paper with FTIR and Raman techniques over a wide range of  $\text{OD}^-$  concentrations.

##### A. Infrared absorption studies

In Figs. 4(a,b) we show for four different  $\text{OD}^-$  concentration absorption measurements at 2.5 K in the region of its first ( $v_0 \rightarrow v_1$ ) and second harmonic ( $v_0 \rightarrow v_2$ ) SM transitions. The actual first harmonic “classical” vibration of isolated  $\text{OD}^-$  defects is expected by the  $\text{OH}^-/\text{OD}^-$  SM frequency ratio ( $1.3565 \pm 0.0002$ ) in other alkali-chloride hosts to lie at about  $2693.5 \pm 1.0 \text{ cm}^{-1}$ . Mostly at lower frequencies than this expected one, we observe several peaks in high  $\text{OD}^-$ -doped crystals, which do not scale linearly with the  $\text{OD}^-$  concentration. Two particular ones, marked in Fig. 4(a) with  $\bullet$  and  $\blacksquare$  symbols, increase approximately with the fourth power of the  $\text{OD}^-$  concentration [Fig. 4(c)]; this in-

dicates that these lines are associated with larger clusters of  $\text{OD}^-$  ions, not with the isolated  $\text{OD}^-$  impurity. An  $\text{OD}^-$ - $\text{OD}^-$  pair line, which corresponds to the line at  $3633 \text{ cm}^{-1}$  for  $\text{OH}^-$ - $\text{OH}^-$  pairs (see Fig. 2), is observed at  $2681 \text{ cm}^{-1}$  with a quadratic concentration dependence.

The nature of these lines was further investigated by quenching the samples from 540 K, a procedure expected to reduce the number of aggregates and increase the number of isolated impurities. An overall reduction of the absorption in the spectral region of  $2670$  to  $2700 \text{ cm}^{-1}$  was observed, but none of the lines in this range increased in intensity. However, we found one rather broad band at  $2707 \text{ cm}^{-1}$  [marked as  $E_2$  in Fig. 4(a)], which appears in the 700 ppm  $\text{OD}^-$  crystal to increase slightly after quenching. Allowing for the difficulty of accurate integration of this broad and weak absorption, its intensity is found to increase roughly linearly with  $\text{OD}^-$  concentration. As this line lies at much higher energy than the expected transition of isolated  $\text{OD}^-$ , we assign it tentatively for a transition between the  $0A_{1g}$  and  $3T_{1u}$  states, corresponding to the  $E_2$  transition observed for  $\text{OH}^-$  (see Figs. 1 and 2). Finer details and the importance of this assignment, will be discussed later after presentation of the  $\text{OD}^-$  Raman results.

In reference to the second harmonic spectra in Fig. 4(b), we expect the frequency of isolated  $\text{OD}^-$  to lie at  $5285 \pm 2 \text{ cm}^{-1}$  (using as before, the frequency ratio of second to first harmonic frequency in other alkali chloride hosts,  $1.9654 \pm 0.0001$ , as a guideline). We see, indeed, in Fig. 4(b) a line at  $5285 \text{ cm}^{-1}$ , the intensity of which increases linearly with concentration as shown in Fig. 4(c); therefore it can be attributed to the  $v_0 \rightarrow v_2$  transition of the isolated  $\text{OD}^-$  defects. It is amazing, however, that no spectral substructure due to the energy-level splitting of  $v_0$  and  $v_2$  can be observed. Though for high concentrations, this could be due to strong interaction effects favoring the classical transition  $B$  (as observed for in first harmonic transition for  $\text{OH}^-$ ), the lack of substructure down to 30 ppm in Fig. 4(b) is not understandable. The broader (partially overlapping) absorption at lower energy around  $5282 \text{ cm}^{-1}$  scaling much stronger with concentration, observed in Fig. 4, is most likely due to  $\text{OD}^-$  aggregates, similarly observed for the first harmonic in Fig. 4(a).

An important additional first and second harmonic measurement was performed on a sample doped with roughly equal amounts of  $^{16}\text{OD}^-$  and  $^{18}\text{OD}^-$ . Motivation for this was the hope that by an oxygen isotope exchange, the undetectable first harmonic  $^{16}\text{OD}^-$  SM transition could become weakly detectable and even reveal, by its spectral fine structure, the involved level structure of  $v_0$  and  $v_1$ . Alas—this hope failed totally in the first harmonic. The observation of a very weak second harmonic with the expected isotopic frequency shift confirmed the presence of  $^{18}\text{OD}^-$  defects, but did not reveal anything new. The physical origins of the extremely weak infrared absorption strength of the  $\text{OD}^-$  in NaCl have so far not been understood, but will be discussed with the SM combination band in Sec. V because the SM transition alone is not allowed by the infrared selection rule.

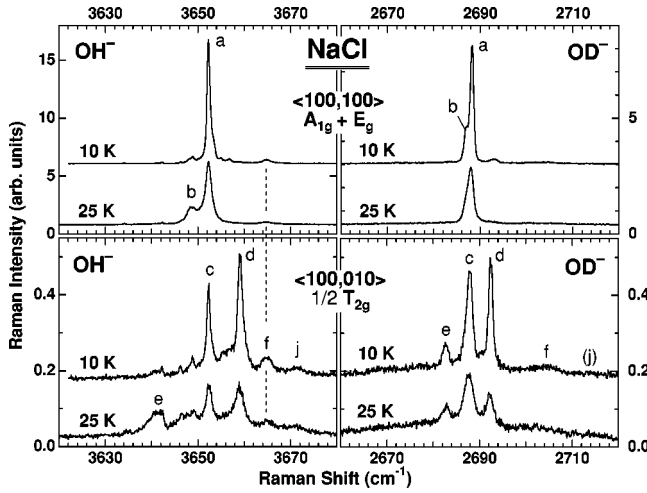


FIG. 5. Comparison of SM Raman spectra for  $\text{OH}^-$  (left) and  $\text{OD}^-$  (right). The  $\text{OH}^-$  concentration was 160 ppm, the  $\text{OD}^-$  concentration 30 ppm. Note the large differences in intensity scale.

### B. Polarized Raman scattering studies

The high-frequency (SM) and low-frequency Raman spectra of  $\text{OD}^-$  are displayed in Figs. 5, 6, and 7, together with  $\text{OH}^-$  spectra for comparison. The  $\text{OH}^-$  spectra are essentially identical to those published by Peascoe and Klein.<sup>13</sup> The low-frequency spectra show  $\nu_0 \rightarrow \nu_0$  transitions, and the high-frequency spectra show  $\nu_0 \rightarrow \nu_1$  transitions. Selection rules determine what transitions are allowed in spectra of  $A_{1g}$ ,  $T_{2g}$ , or  $E_g$  symmetry, and are a considerable help for interpretation. Table I gives an overview of the observed

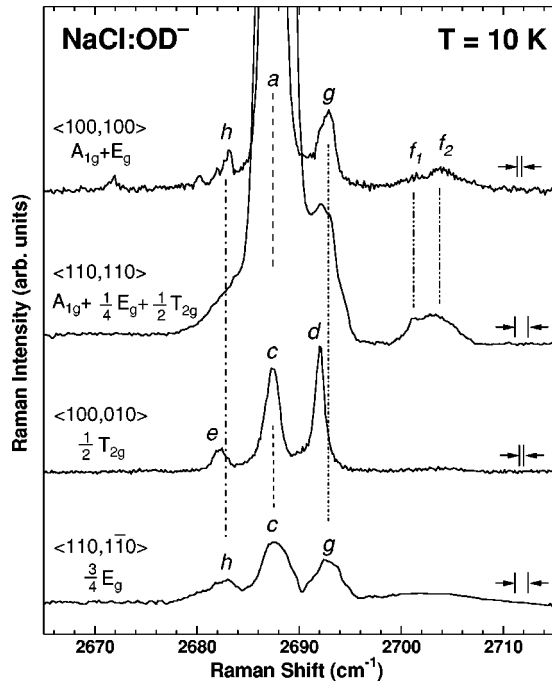


FIG. 6. SM Raman transitions of  $\text{OD}^-$  in different symmetries. Spectra were recorded from a sample with 200 ppm  $\text{OD}^-$ . The 1st and 3rd spectra have been recorded in high resolution, the 2nd and 4th in low resolution.

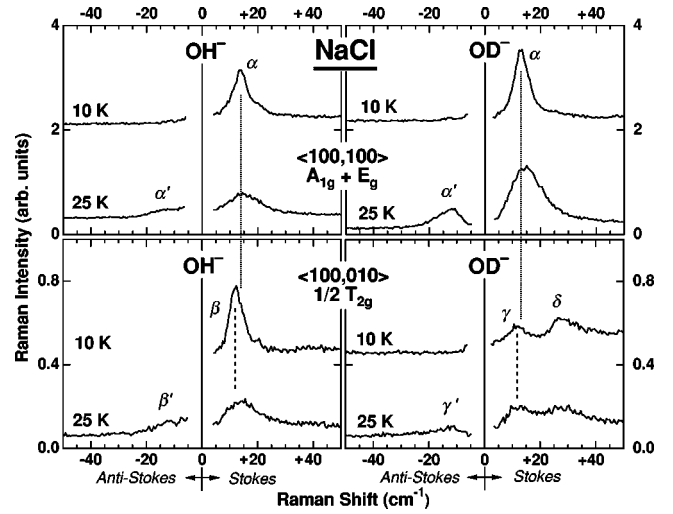


FIG. 7. Comparison of low-frequency Raman spectra for  $\text{OH}^-$  (left) and  $\text{OD}^-$  (right). The  $\text{OH}^-$  concentration was 160 ppm, the  $\text{OD}^-$  concentration 200 ppm. Note the factor four difference in intensity scale for the two polarizations.

transitions, and the second column shows in which symmetries a transition is Raman allowed. The problem of analysis is further simplified because at low temperatures, only the lowest levels in the SM ground state are significantly populated.

The most convenient way to identify the peaks is to start with the high-frequency spectra in Fig. 5. The main peak *a* in the  $A_{1g} + E_g$  spectrum is the  $0A_{1g} \rightarrow 0A_{1g}$  transition, at the fundamental frequency of the stretch mode vibration. Other

TABLE I. Overview of the  $\text{OH}^-$  and  $\text{OD}^-$  Raman transitions. The first part of the table describes the  $\nu_0 \rightarrow \nu_1$  transitions, and the listed frequencies are all relative to the  $0A_{1g} \rightarrow 0A_{1g}$  line. For  $\text{OH}^-$  this is at  $3651.7 \text{ cm}^{-1}$ , and for  $\text{OD}^-$  at  $2687.2 \text{ cm}^{-1}$ .

Transition	Symmetry	Label	$\text{OH}^-$	$\text{OD}^-$
$\nu_0 \rightarrow \nu_1$				
$3T_{1u} \rightarrow 1T_{1u}$	$E_g, T_{2g}$			
$2T_{2g} \rightarrow 0A_{1g}$	$T_{2g}$	e	-11.0	-5.5
$2T_{2g} \rightarrow 2E_g$	$T_{2g}$			
$2T_{2g} \rightarrow 2T_{2g}$	$A_{1g}, E_g, T_{2g}$	b	-3.7	-1.2
$2E_g \rightarrow 0A_{1g}$	$E_g$	b,h	-3.3	-4.9
$3T_{1u} \rightarrow 3T_{1u}$	$A_{1g}, E_g, T_{2g}$			
$0A_{1g} \rightarrow 0A_{1g}$	$A_{1g}$	a	0.0	0.0
$1T_{1u} \rightarrow 1T_{1u}$	$A_{1g}, E_g, T_{2g}$	c	0.0	-0.3
$2E_g \rightarrow 2E_g$	$A_{1g}, E_g$		0.9	
$2E_g \rightarrow 2T_{2g}$	$T_{2g}$			
$0A_{1g} \rightarrow 2E_g$	$E_g$	g	4.5	5.1
$0A_{1g} \rightarrow 2T_{2g}$	$T_{2g}$	d	6.8	4.2
$1T_{1u} \rightarrow 3T_{1u}$	$E_g, T_{2g}$	f	12.7	16.2
$2T_{2g} \rightarrow 4T_{2g}$	$E_g, T_{2g}$	j	19.1	24 ?
$\nu_0 \rightarrow \nu_0$				
$1T_{1u} \rightarrow 3T_{1u}$	$E_g, T_{2g}$	$\alpha, \gamma$	13.6	12.8
$0A_{1g} \rightarrow 2T_{2g}$	$T_{2g}$	$\beta$	11.9	
$2T_{2g} \rightarrow 4T_{2g}$	$E_g, T_{2g}$	$\delta$		26

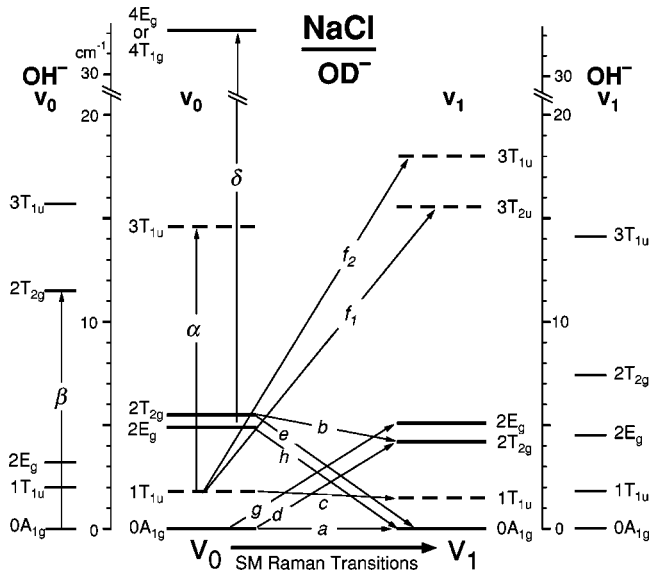


FIG. 8. The part between the scales shows the  $v_0$  and  $v_1$  levels of  $\text{OD}^-$  in NaCl, constructed from the polarized Raman transitions at low ( $\alpha$ ) and high frequency ( $a, b, \dots, f$ ). Though  $\alpha$ ,  $f$ , and  $c$  determine the relative energies of the ungerade  $1T_{1u}$  and  $3T_{1u}$  states, their energies relative to the gerade states was determined from the  $0A_{1g} \rightarrow 3T_{1u}$  IR SM transition. On both sides, outside the energy scales, the  $v_0$  and  $v_1$  levels of  $\text{OH}^-$  are plotted for direct comparison with the equivalent ones for  $\text{OD}^-$ .

transitions between states of identical symmetry are also  $A_{1g}$  allowed, and because the levels are not equidistant in the  $v_0$  and  $v_1$  states, the peak becomes asymmetric. At the low-frequency side, the  $2T_{2g} \rightarrow 2T_{2g}$  transition can clearly be distinguished as a shoulder  $b$  on the main line.

The  $1/2T_{2g}$  spectra are basically similar for both isotopes, however not in the size of their splittings. At low temperatures, there is a strong central peak  $c$  that has a slightly lower frequency than the  $0A_{1g} \rightarrow 0A_{1g}$  transition. For  $\text{OH}^-$ , this has been attributed to the  $1T_{1u} \rightarrow 1T_{1u}$  transition, and it is likely to be the same for  $\text{OD}^-$ . In both cases this peak is surrounded by transitions  $d$  and  $e$  between the  $2T_{2g}$  and  $0A_{1g}$  states. These are not equidistant from the central peak, again, because the level splitting is different in the ground and excited state. The main change from  $\text{OH}^-$  is the strong decrease of the frequency shift for  $\text{OD}^-$ ; if we put these transitions into a level diagram as in Fig. 8, we see that the  $T_{2g}$  level in the ground-state  $v_0$  is much lower for  $\text{OD}^-$  than for  $\text{OH}^-$ .

As the temperature increases and the higher-energy levels in the  $v_0$  state become populated, the ratio between the  $d$  and  $e$  peaks changes. A quantitative analysis of this could also yield a confirmation of the splitting between the  $2T_{2g}$  and  $0A_{1g}$  levels. Unfortunately, the local heating by the focused laser beam results in a considerable uncertainty on the exact temperature dependence. Local temperatures determined from low-frequency Stokes and anti-Stokes Raman spectra were 5 to 10 K higher than the heat-exchanger temperature, depending on laser power, sample quality, and the presence of lattice defects. Our rather uncertain estimate for the acti-

vation energy is  $3.9 \text{ cm}^{-1}$ , while the spectral position of the lines indicates that the  $2T_{2g}$  level is at  $5.5 \text{ cm}^{-1}$ .

To locate the  $2E_g$  level, we have to identify the  $0A_{1g} \leftrightarrow 2E_g$  transitions. These have  $E_g$  symmetry, and to distinguish them from any  $A_{1g}$  lines, we recorded a  $3/4E_g$  spectrum. Figure 6 shows the  $3/4E_g$ ,  $1/2T_{2g}$ , and  $A_{1g} + E_g$  spectra on a similar intensity scale. The signal noise/ratio of the sample polished to have  $\langle 110 \rangle$  surfaces was considerably worse than that of cleaved samples; therefore, these spectra were recorded in the low-resolution mode of the spectrometer, and were smoothed afterwards. The  $0A_{1g} \leftrightarrow 2E_g$  transitions  $h$  and  $g$  are at slightly different positions from the  $0A_{1g} \leftrightarrow 2T_{2g}$  transitions  $e$  and  $d$ , and Fig. 8 shows the consequences of this: In the  $v_0$  state, the  $2E_g$  and  $2T_{2g}$  levels are now very close, while for  $\text{OH}^-$  they were separated by  $8.3 \text{ cm}^{-1}$ . In the  $v_1$  state, the order of the  $2E_g$  and  $2T_{2g}$  levels even appears to have been reversed.

In the  $A_{1g} + E_g$  spectra for  $\text{OH}^-$ , two wide, low peaks can just be seen on the high-frequency side of  $d$ . One of them,  $f$ , was identified in Ref. 13 as the  $1T_{1u} \rightarrow 3T_{1u}$  transition. In the  $\text{OD}^-$  spectra only a single peak  $f$  is visible in this range, although it is slightly asymmetric. We assign this to the  $1T_{1u} \rightarrow 3T_{1u}$  transition, but it is possible that it overlaps with other transitions.

Based on this interpretation of the high-frequency spectra, we can now analyze the low-frequency spectra of Fig. 7. These are, of course, limited at the low-frequency side by the presence of the strong laser line, and although we plot spectra starting from about  $5 \text{ cm}^{-1}$ , we expect considerable distortion of the spectra in the range  $5\text{--}8 \text{ cm}^{-1}$ .

The  $A_{1g} + E_g$  spectra for  $\text{OH}^-$  and  $\text{OD}^-$  are quite similar, because they are both dominated by a single strong transition  $\alpha$ , which at 10 K is only visible in Stokes scattering, but at 25 K is also visible in anti-Stokes scattering ( $\alpha'$ ). This is the  $1T_{1u} \rightarrow 3T_{1u}$  transition, and it is at slightly lower frequency for  $\text{OD}^-$ . For  $\text{OH}^-$ , a shoulder on this  $\alpha$  transition at  $21 \text{ cm}^{-1}$  has been identified as the  $2E_g \rightarrow 4A_{1g}$  transition,<sup>13</sup> but for  $\text{OD}^-$  we cannot confirm its presence.

The  $T_{2g}$  spectra on the other hand are quite different. The  $\text{OH}^-$  spectrum shows a single strong peak  $\beta$  corresponding to the  $0A_{1g} \rightarrow 2T_{2g}$  transition, with its anti-Stokes equivalent  $\beta'$ . From the high-frequency spectra, we determined that the  $2T_{2g}$  level is quite a bit lower for  $\text{OD}^-$ , probably below the frequency range in which we can collect reliable data. Indeed, no corresponding  $\beta$  peak has been observed for  $\text{OD}^-$ . A very small peak  $\gamma$  remains at the expected position, and a somewhat stronger peak  $\delta$  is now seen at  $27 \text{ cm}^{-1}$ . The unwanted presence of about 5 ppm of  $\text{OH}^-$  in this  $\text{OD}^-$ -doped sample could partly account for  $\gamma$ , and besides this one also expects to see something of the  $1T_{1u} \rightarrow 3T_{1u}$  transition  $\alpha$  in  $1/2T_{2g}$  spectra.  $\gamma$  may therefore have several components. A careful comparison shows that the  $\delta$  peak at  $27 \text{ cm}^{-1}$  is present in both  $1/2T_{2g}$  and  $A_{1g} + E_g$  Raman spectra, but in the latter, is almost completely buried under the strong  $\alpha$  peak. The implication is that this is a transition between two  $T$ -type states, maybe  $2T_{2g} \rightarrow 4T_{1g}$ .

### C. Construction of models from observations

From these observations and interpretation, we can derive the  $\text{OD}^-$  level diagram shown at the center of Fig. 8 in

comparison to the  $\text{OH}^-$  levels at the outside. In contrast to the large effect of the hydrogen isotope variation, the  $^{16}\text{O} \rightarrow ^{18}\text{O}$  isotope substitution produced no measurable difference in IR and Raman measurements.

A limitation inherent in Raman spectroscopy is that there are no allowed transitions between gerade and ungerade states. Therefore, we have two sets of levels, but cannot conclude anything about the relative position of these. The near- and far-infrared absorptions are, of course, the best source of information about the relative position of gerade and ungerade states as shown to be the case of  $\text{OH}^-$ . For  $\text{OD}^-$ , however, we have seen in Fig. 4(a) of Sec. IV A, only one weak broadband that could be identified as an absorption line of isolated  $\text{OD}^-$ . In parallel to the observed SM absorptions of  $\text{OH}^-$  shown in Fig. 1 and 2, we assign tentatively this only available broad  $\text{OD}^-$  absorption to the  $0A_{1g} \rightarrow 3T_{1u}$  transition or  $E_2$  band. This determines the energy position of the  $3T_{1u}$  level in the  $v_1$  state, and via the observed Raman transitions  $\alpha$ ,  $f$ , and  $c$  also the position  $1T_{1u}$  in both  $v_0$  and  $v_1$  as well as  $3T_{1u}$  in the  $v_0$  state. We indicate in Fig. 8 the still existing uncertainty about relative positions of gerade and ungerade states by dashed lines for the latter. If these lines are valid, the lowest tunneling splitting  $\Delta_1$  between  $0A_{1g}$  and  $1T_{1u}$  would have become slightly reduced by the  $\text{OH}^- \rightarrow \text{OD}^-$  isotope exchange.

We can be much more confident about the changes of splittings between the gerade states, all determined by polarized Raman scattering. The splitting  $\Delta_2$  between  $0A_{1g}$  and  $2E_g$  increases considerably by the  $\text{OH}^- \rightarrow \text{OD}^-$  isotope exchange for both  $v_0$  and  $v_1$  state to values of  $\Delta_2 = 4.9$  and  $\Delta_2^* = 5.1 \text{ cm}^{-1}$ , respectively. Even more obvious is the decrease of the  $\Delta_3$  splitting between  $0A_{1g}$  and  $2T_{2g}$  by the isotope exchange, strong enough to bring in the  $v_1$  state the  $2T_{2g}$  level below the  $2E_g$  level, i.e., make  $\Delta_3^*$  smaller than  $\Delta_2^*$ .

How do our new  $\text{OD}^-$  results fit into the empirical models proposed and used earlier for the motional behavior of  $\text{OH}^-$  in  $\text{NaCl}$ ? Obviously, we start with the Devonshire approach that was successfully employed for the Raman results in Ref. 13. Figure 9 shows for this model, the energies and symmetries of hindered rotational states, produced from the free rotor states by an increasing  $V_4$  potential (with both energy  $E$  and potential strength  $K$  in units of the rotational constant  $B = \hbar^2/2I$  of the system). We try to fit into this diagram the results of Fig. 8 for our “sequence” of four systems [ $v_0(\text{OH}^-) \rightarrow v_1(\text{OH}^-) \rightarrow v_0(\text{OD}^-) \rightarrow v_1(\text{OD}^-)$ ] in two different ways:

(a) A very good fit of the four lowest levels (LL) can be achieved for each case, however, only by assuming a rather strong gradual decrease of the  $B$  values along the sequence of systems [see Fig. 9(a)]. While this achieves a good fit also to the high levels (HL) of  $v_0(\text{OH}^-)$ , increasingly stronger deviations between measured and predicted HL values (indicated by arrows) develop along the sequence of systems.

(b) In the same diagram [plotted in Fig. 9(b) in opposite  $K$  direction] we keep the  $B$  value of  $v_0(\text{OH}^-)$  constant for all

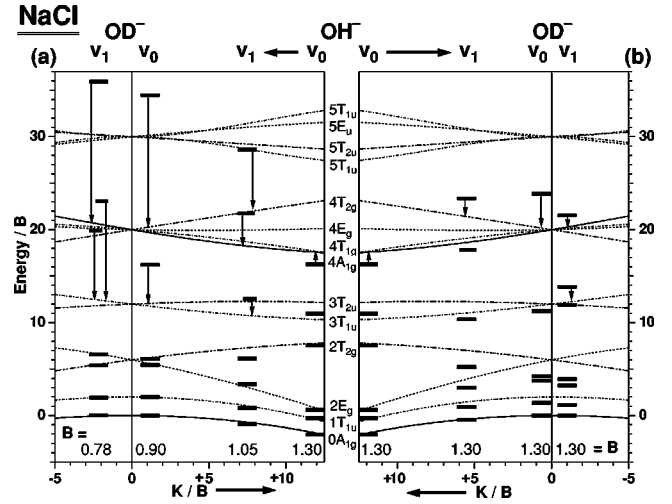


FIG. 9. The obtained  $v_0$  and  $v_1$  energy levels of  $\text{OH}^-$  and  $\text{OD}^-$  (horizontal bars), plotted by best fit of the lowest levels into a simple  $V_4$  Devonshire diagram. The vertical arrows indicate deviations of the experimental data from the model. For all four cases, the  $B$  value chosen for the fit is indicated.

systems. In contrast to (a), now the LL’s show increasing deviations and the HL’s a good fit along the sequence of systems.

For both fitting processes (a) and (b), the “starting-point” (in the middle of Fig. 9) is the  $v_0(\text{OH}^-)$  system, for which all energy levels can be fitted by a single chosen  $B$  value. In contrast to process (a), this  $B$  value can be preserved in (b) for the other systems, to fit at least all their HL states. This makes  $B = 1.3 \text{ cm}^{-1}$  and its related moment of inertia  $I = \hbar^2/2B = 13 \text{ amu } \text{Å}^2$  the best common fitting parameter shared by all four systems. Restricting it (without any “dressing” by surrounding lattice distortions) to only the “bare molecule,” its large value is equivalent to the rotation of the oxygen about a point on the  $\text{OH}^-$  bond length of  $0.96 \text{ Å}$ , very close ( $0.06 \text{ Å}$ ) to the hydrogen. This is of course confirmation of a large off-center shift of the molecular center of mass. In its rotation around the vacancy, the adiabatically following molecular reorientation around its own c.m. contributes only very little ( $\sim 6\%$ ) to the total value of  $I$ . The slight opposite changes in the two contributions by the  $\text{OH}^-/\text{OD}^-$  isotope exchange compensate each other and keep the total  $I$  constant. The minute increase ( $\sim 0.02 \text{ Å}$ ) of bond length between  $v_0$  and  $v_1$  due to weak SM anharmonicity is even more negligible for the total  $I$ .

We choose (b) as the more correct description, because it yields for all our systems, a good fit of their HL states, and the assumption of a constant  $B$  value seems physically correct. Its deficiency, the increasing misfit of LL states along our sequence of systems, could possibly be removed by a well-justified extension of the Devonshire model. The use of only the first term  $V_4$  of the expansion of the potential in spherical harmonics<sup>17</sup> is surely a drastic simplification. As Beyeler<sup>22</sup> showed, this yields only  $\langle 100 \rangle$  and  $\langle 111 \rangle$  orientations, and in order to model  $\langle 110 \rangle$  orientations, one has to at least include also the next term,  $V_6$ . By continuous variation of the potential  $V = K(V_4 \cos \phi + V_6 \sin \phi)$  through all mixing

angles  $\phi$ , a wide variation of potential shapes and related eigenstates is encountered. For a fixed  $\langle 100 \rangle$  orientation, the  $V_4$  contribution is surely dominant, but as we move progressively towards a free rotation, there is an increasing probability of other orientations, e.g., the  $\langle 110 \rangle$  orientations linked to the  $V_6$  potential that represents interaction with the next-nearest neighbors. While lowering  $K$  of course reduces all the barriers for reorientation, admixture of small  $V_6$  contributions has the effect of lowering the barriers in specific directions. For a positive  $V_6$  admixture, the barriers in the  $\langle 110 \rangle$  direction are reduced, while those in the  $\langle 111 \rangle$  directions increase. For a negative  $V_6$  admixture, the  $\langle 110 \rangle$  barriers are increased, but new minima develop in the  $\langle 111 \rangle$  directions. Better fittings of our results might be achieved by a properly chosen  $V_4/V_6$  mixture, compared to the simple  $V_4$  model (b) that allows only a variation of the parameter  $K$ .

A weakness of the application of the Devonshire model is that it does not actually use the size of the off-center shift as a parameter. The translational tunneling model proposed by Suto and Ikezawa<sup>20</sup> employs a LCAO-MO calculation, using the off-center shift and the shape of double parabolic potential wells as parameters. As we have seen in Sec. III A, this model explains the  $\nu_0(\text{OH}^-)$  levels well. It also offers quite a good prediction of the  $\nu_1(\text{OH}^-)$  levels, if a smaller off-center shift is assumed. On the other hand, from the level diagram presented in Ref. 20, it is evident that different potential parameters have to be used to fit the  $\text{OD}^-$  levels. Because this model is essentially a phenomenological one, offering no physical interpretation of its potential parameters, we cannot evaluate how these parameters should change under the  $\text{H} \rightarrow \text{D}$  substitution. The model also ignores the orientation of the molecular axis, which still may be an important parameter.

The ideal, but alas unavailable, theoretical model would calculate the potential strength for all angular and radial coordinates on the basis of the best microscopic model for interionic polarization and repulsion effects. A recent approach with a shell model<sup>23</sup> has achieved quite good agreement with experiment for positive and negative point ion defects on  $\langle 111 \rangle$  or  $\langle 110 \rangle$  off-center positions. The large effects of small changes in parameters like interionic distance (experimentally verifiable by compression experiments) illustrate the difficulty of these calculations. Evidently, an off-center molecular defect such as  $\text{OH}^-$  or  $\text{OD}^-$  would be even more difficult to calculate because it has an additional angular parameter, the orientation of the molecular axis relative to the off-center shift.

Disregarding this, one might take the similarly sized  $\text{F}^-$  ion as a first rough approximation of the  $\text{OH}^-$ . For  $\text{F}^-$  in several hosts, an  $\langle 110 \rangle$  off-center shift has been predicted and experimentally confirmed. The  $\text{OH}^-$  instead shifts in the  $\langle 100 \rangle$  direction. This may be caused by its electronic-dipole moment and the bonding of the molecule with the nearest-neighbor  $\text{Na}^+$  cation, forming the resemblance of a linear  $\text{NaOH}$  molecule.<sup>24</sup> The Na-O bond length of the free  $\text{NaOH}$  molecule agrees very well with the determined off-center shift of the oxygen atom towards the nearest-neighbor  $\text{Na}^+$

cation in the  $\text{NaCl}$  lattice; while the bending mode of the not so rigid Na-O bond matches closely the librational frequency of the impurity.

On the other hand, for our weak potentials we expect a significant probability to find the  $\text{OH}^-$ , and even more so, the  $\text{OD}^-$  oriented in other directions than  $\langle 100 \rangle$ . So, an ideal model should also give information about the existence and energy of potential wells in  $\langle 110 \rangle$  or  $\langle 111 \rangle$  orientations, their distance from the center of the vacancy, and their possible role in the reorientation process. It is even conceivable that the orientation of the molecule may not always follow the off-center shift during the weakly hindered reorientation process, as was assumed in all models.

We must conclude that there remains considerable work to be done for the development of a viable microscopic model of the  $\text{OH}^-$  and  $\text{OD}^-$  in  $\text{NaCl}$ . So far, models have been constructed that, by a suitable choice of parameters, can fit the levels quite well for each isotope and each vibrational state. What is now required is a model that can explain, with valid and convincing physical arguments, the main result of this paper: The systematic decrease of the strength of the orientational potential for the sequence  $\nu_0(\text{OH}^-) \rightarrow \nu_1(\text{OH}^-) \rightarrow \nu_0(\text{OD}^-) \rightarrow \nu_1(\text{OD}^-)$ , producing a change from weakly hindered to quasi-free rotation along the sequence.

## V. $\text{OH}^-$ AND $\text{OD}^-$ LIBRATION AND PHONON COUPLING

Beyond the study of the low-energy motional states, our Raman and FTIR measurements yield informations about the high-energy libration and the phonon coupling of our molecular defects. Similarly, as in the case of motional states, these features can be studied with Raman as “fundamental transitions” in the  $\nu_0$  state, or by Raman and FTIR as combination transitions of SM in the  $\nu_1$  state of  $\text{OH}^-$  and  $\text{OD}^-$ .

### A. Fundamental transitions

The librational mode of the  $\text{OH}^-$  has been previously observed by IR absorption at  $395 \text{ cm}^{-1}$  together with a strong phonon sideband at a  $\sim 100 \text{ cm}^{-1}$  higher energy.<sup>18,26</sup> Uniaxial stress alignment of  $\text{OH}^-$  has confirmed by elasto-optical studies,<sup>27</sup> that this IR librational transition was polarized as expected perpendicular to the molecular axis and SM transition of the  $\langle 100 \rangle$  oriented cigar-shaped  $\text{OH}^-$  elastic-dipole tensors. The libration of  $\text{OD}^-$  cannot be detected or studied this way, as its frequency is totally covered by the strong intrinsic phonon absorption of the  $\text{NaCl}$  host.

Our attempts to observe the  $\text{OH}^-$  or  $\text{OD}^-$  librational mode in the expected  $T_{2g}$  symmetry by Raman scattering were unsuccessful. For this case, the two librational frequencies are overlapped by the second-order two-phonon Raman spectrum of the host. In spite of this, however, both  $\text{OH}^-$  and  $\text{OD}^-$  librations could be well detected on top of this background as strong extra bands in  $\text{KCl}$ ;<sup>28,29</sup> this is in contrast to our  $T_{2g}$  Raman measurement in  $\text{NaCl}$  at 10 K, in

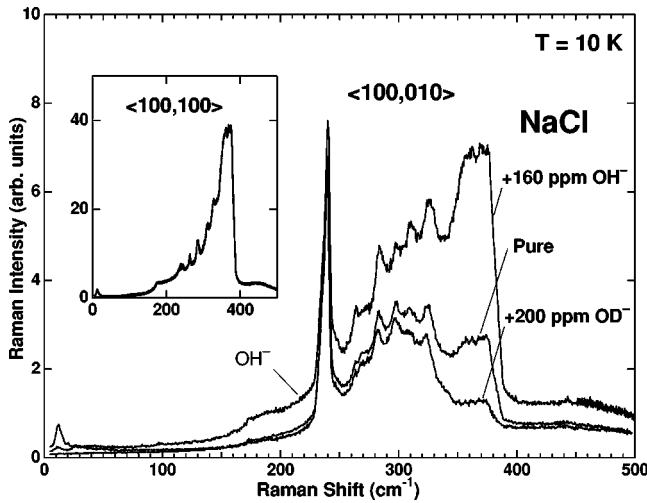


FIG. 10. Second order  $\langle 100,010 \rangle 1/2T_{2g}$  Raman spectra measured at 10 K in three NaCl crystals: One pure, one doped with 160 ppm  $\text{OH}^-$ , and one doped with 200 ppm  $\text{OD}^-$ . The plotted strength of each of the three spectra was obtained by normalization of its corresponding  $\langle 100,100 \rangle$  spectrum (shown in the inset) which in all three cases has identical spectral shape.

which, for  $\text{OH}^-$  and  $\text{OD}^-$  concentrations up to 1000 ppm, no spectral librational mode could be identified.

Instead, we observed a behavior, illustrated in Fig. 10, that is totally unexpected and difficult to explain because it does not seem to be related in a predictable way to impurity concentration: For all pure or  $\text{OH}^-/\text{OD}^-$  doped samples, the  $A_{1g} + E_g$  second-order phonon scattering spectra are identical in spectral shape and within experimental accuracy of similar intensity, as expected. In contrast to this, the spectral shape and relative intensity of the corresponding  $1/2T_{2g}$  spectra vary quite strongly in the range of 250 to 400  $\text{cm}^{-1}$  without any modes attributed to  $\text{OH}^-$  or  $\text{OD}^-$ : It appears that it is merely the  $T_{2g}$  second order phonon scattering that is strongly sample-dependent in this frequency range. When using the identical  $A_{1g} + E_g$  spectra for intensity calibration (see inset of Fig. 10), differences of up to a factor five in intensity are found, with the least intense spectrum originating from a sample doped with a 200 ppm of  $\text{OD}^-$  and the strongest spectrum from one doped with 160 ppm of  $\text{OH}^-$ . An increase of the  $\text{OH}^-$  and  $\text{OD}^-$  concentration in the sample appears to reduce the magnitude of the above variations, which makes it hard to assume a direct link to the  $\text{OH}^-$  or  $\text{OD}^-$  impurities.

Apart from the low-lying motional states discussed in Secs. III and IV, we observe (after subtraction of the intrinsic second-order Raman background) very weak one-phonon spectra induced by the  $\text{OH}^-$  and  $\text{OD}^-$  impurities: for  $A_{1g} + E_g$  symmetry, a broad spectrum in the 50 to 250  $\text{cm}^{-1}$  range in rough similarity to the phonon-density spectrum; for  $T_{2g}$  symmetry, mostly a pronounced single peak near 190  $\text{cm}^{-1}$  (of width 14  $\text{cm}^{-1}$  at 10 K). Both these spectra are isotope independent, indicating that they are due to the coupling of both isotopes to rather normal or localized phonons. As they scale more than quadratically with  $[\text{OH}^-]$  and

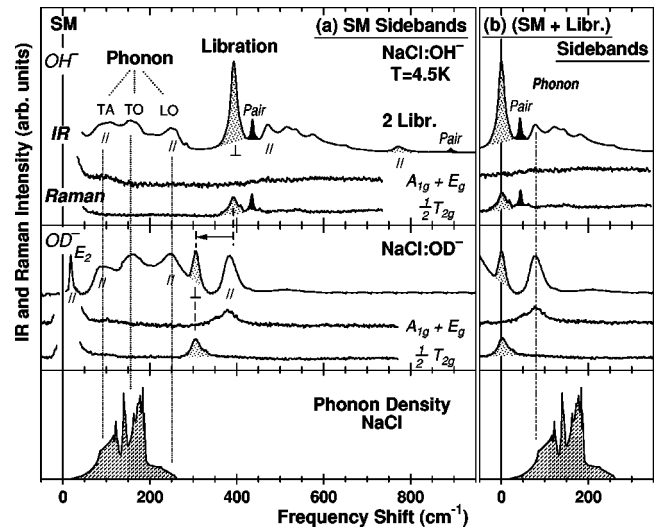


FIG. 11. (a) SM sideband spectra of  $\text{OH}^-$  and  $\text{OD}^-$  in NaCl at 4.5 K, plotted in frequency relative to the SM. While phonon sidebands (shown in comparison to the NaCl phonon density from Ref. 25) are the same for  $\text{OH}^-$  and  $\text{OD}^-$ , the specially marked librational sideband shows strong isotope shift. (b) Sideband spectra of (SM + Libr.) for  $\text{OH}^-$  and  $\text{OD}^-$ , showing their own phonon sidebands, compared again to the phonon density. Details about the indicated symbols  $\parallel$  and  $\perp$ , SM and librational absorptions of pairs, and 2nd harmonics of librational bands are discussed in the text.

$[\text{OD}^-]$ , they could be attributed to the phonon coupling of pairs or clusters. For a possible alternative interpretation, see Sec. VI.

## B. Combination transitions

Sideband spectra of the SM mode, which show transitions involving excitation of the SM plus at least one other mode, contain more information. Despite the nonobservable, ultra-weak SM absorption strength of the isolated  $\text{OD}^-$  defect, its sidebands are still present with an intensity comparable to that found for  $\text{OH}^-$ . Therefore, some of the IR SM properties of  $\text{OD}^-$  can be studied “indirectly” by measuring it in combination with other modes.

Figure 11 gives an overview of the sideband spectra, both for IR absorption and Raman scattering. For clarity, we removed from this plot the complicated and out-of-scale structure in the SM spectral region of  $\text{OH}^-$  (as shown in Figs. 2, 5, and 6), and retained for  $\text{OD}^-$  only the  $E_2$  band associated with a low-energy transition of isolated  $\text{OD}^-$  (see Fig. 4). The impurity concentrations of the samples in Fig. 11 are 1000 ppm for  $\text{OH}^-$  and 700 ppm for  $\text{OD}^-$ , but for convenience, their IR spectra have been plotted in different vertical scales. All sidebands, except the ones marked “pair,” increase essentially linearly with concentrations of  $\text{OH}^-$  or  $\text{OD}^-$ , assuring that they originate from isolated defects. The IR absorption spectra show more bands than the Raman spectra, so we will begin with their discussion.

*Phonon sidebands* with three broad components are observed in the range of 50–300  $\text{cm}^{-1}$  from the SM band, and are very similar for  $\text{OH}^-$  and  $\text{OD}^-$  impurities. The three components in IR absorption correspond closely to the TA,

TO, and LO phonons of the theoretical phonon density. Any possible existing local modes induced by hydroxide impurities are not well separated from the host phonons.

*Librational sidebands* with narrow Lorentzian shapes, in the spectral region above the phonon sidebands, are observed at  $+393\text{ cm}^{-1}$  for  $\text{OH}^-$  and for the first time, at  $+303\text{ cm}^{-1}$  for  $\text{OD}^-$ . The librational frequency reduces under  $\text{OH}^- \rightarrow \text{OD}^-$  substitution by a factor 1.30, slightly smaller than the theoretical prediction 1.374 for the rotation of free  $\text{OH}^-$  and  $\text{OD}^-$  molecular ions. This indicates that the center of librational motion lies rather close to the c.m., and will contain only a weak dressing effect on this angular motion.

For  $\text{OH}^-$  with a much stronger librational sideband, a weak *second harmonic libration* is also observable at  $+773\text{ cm}^{-1}$ . Since the frequency is close to twice the first harmonic, the librational potential wells are expected to be very close to simple harmonic functions, at least up to  $800\text{ cm}^{-1}$ . From this observation, the potential barrier height for rotation around the c.m. can be estimated to be very high ( $>1000\text{ cm}^{-1}$ ). For the high-doped  $\text{OH}^-$  samples, a sharper first- and second-order librational band of pairs are also detectable (marked black in Fig. 11).

Additional combination bands are observed above the librational sidebands. Though their frequency shifts from the SM are different for  $\text{OH}^-$  and  $\text{OD}^-$  [Fig. 11(a)], they become essentially the same when plotted as shifts from the librational sidebands [Fig. 11(b)]. We therefore interpret them as a *phonon sideband spectrum of the SM + libration transition*. This shows, by comparison to the phonon density, strong coupling to acoustic phonons around  $80\text{ cm}^{-1}$ . It is similar to the  $\sim 100\text{ cm}^{-1}$  higher phonon sideband, observed at the fundamental librational absorption.<sup>26</sup>

The *symmetries* of the sidebands are studied in comparison to the SM absorption dichroism under  $\langle 100 \rangle$  uniaxial stress, produced by paraelastic alignment of the molecular defects. First, the  $\text{OH}^-$  defects are confirmed to have cigar-shaped elastic-dipole tensors of  $\langle 100 \rangle$  orientation by these experiments. Compared to this SM dichroism direction, the symmetries of the sidebands are shown in Fig. 11, marked with // (parallel to SM) or  $\perp$  (perpendicular to SM). Only the stress dichroism of the first harmonic librational sideband is perpendicular to that of the SM, while the second harmonic of the libration is parallel to the SM, both as expected. All the observed SM phonon-sideband transitions are mostly polarized // to the SM.

For the same samples, a number of transitions can also be seen in Raman scattering, as illustrated in Fig. 11 with Raman spectra recorded with  $\langle 100 \rangle$  and  $\langle 010 \rangle$  polarization, under  $\langle 100 \rangle$  laser excitation. The librational sideband is clearly observed for both  $\text{OH}^-$  and  $\text{OD}^-$ , and in the first case, the libration of pairs is also observed. All phonon sidebands are very weak and barely detectable with the exception of the SM + libration + phonon sideband for  $\text{OD}^-$ , which is clearly observed. This band does not have the complicated shape of the other phonon sidebands, suggesting that only selected phonons couple, in a strong way, to this particular librational mode. The symmetries of the sidebands can be determined by the polarization of the Raman-scattered light, without any application of external fields (elastic stress or

TABLE II. The upper part of the table gives the integrated IR absorption intensities of  $\text{OH}^-$  and  $\text{OD}^-$  in NaCl hosts at 4.5 K, in units of  $\text{cm}^{-2}$  per 1000 ppm. The symbols of // and  $\perp$  stand for polarization of transition relative to that of the SM. The lower part gives the corresponding integrated Raman intensities at 10 K, in arbitrary units. To compare Raman spectra from different measurements and samples, the spectra were normalized to the peak intensity of the parallel polarized second-order phonon scattering of the host.

Infrared absorption	$\text{OH}^-$	$\text{OD}^-$	$\text{OH}^-/\text{OD}^-$
SM all (//)	40	$<0.3$	$>120$
SM $E_2$ (//)	1.2	0.2	6
SM + Phonon (//)	16	6.5	2.5
SM + Libration ( $\perp$ )	10	0.7	14
SM + Libration + Phonon (//)	10	1.2	8
SM + 2 Libration (//)	0.7		
<b>Raman Scattering</b>	$\text{OH}^-$	$\text{OD}^-$	$\text{OH}^-/\text{OD}^-$
SM ( $A_{1g}+E_g$ )	58	31	1.9
SM ( $1/2T_{2g}$ )	5.9	6.6	0.9
SM + Libration ( $1/2T_{2g}$ )	0.37	0.39	0.9
SM + Libration + Phonon ( $A_{1g}+E_g$ )		0.53	

electric) as required in infrared techniques. The librational sideband appears, as expected,<sup>29</sup> in the  $1/2T_{2g}$  spectra. Its phonon sideband appears in the parallel polarized  $A_{1g}+E_g$  spectra.

The *strengths* of the SM and all its combination bands measured with IR absorption or Raman for  $\text{OH}^-$  and  $\text{OD}^-$ , and their ratio under isotope variation, are summarized in Table II. It is important to realize that a ‘‘pure’’  $\nu_0 \rightarrow \nu_1$  SM transition is allowed only for Raman in  $A_{1g}$  symmetry, while all  $T_{2g}$  and  $E_g$  Raman and the IR-absorption transitions require a combination of SM with allowed transitions between the low-energy motional states of  $\nu_0$  and  $\nu_1$ . In our Raman experiments, we observe the SM without or with motional transitions at about equal strengths for the  $\text{OH}^-$  and  $\text{OD}^-$  in NaCl. This shows (as expected) that the electronic polarizability tensor and its derivative to the relevant normal coordinates is basically independent of  $\text{OH}^- \rightarrow \text{OD}^-$  isotope variation.

This rather simple Raman behavior is in strong contrast to that of the IR absorption, for which an extremely high ratio (of  $>120$ ) is observed for the strength of the (SM + motional) transitions of  $\text{OH}^-$  and  $\text{OD}^-$ . This could, in principle, be interpreted by a very small derivative of the  $\text{OD}^-$  electric-dipole moment  $(dp/dr)_{r_0}$  at its equilibrium distance  $r_0$ , in contrast to a larger one for  $\text{OH}^-$ . However, a second significant result must also be considered: far IR direct absorption transitions between motional energy levels in the  $\nu_0$  state are well observable for  $\text{OH}^-$  but *not detectable* for  $\text{OD}^-$ .<sup>14</sup> Even if ‘‘the reason for the absence of any  $\text{OD}^-$  induced far IR absorption is not understood’’ (as quoted from Ref. 14), it could be the same one responsible for the absence of near IR- $\text{OD}^-$  (SM + motional) absorption. Though unable to offer new physical explanations, we follow this scheme and choose not SM itself but its ‘‘combination partner’’ motional

transitions, as the culprit for its nondetectable strength. We check the approximate validity of this choice by the relative isotopic strength of two other SM combination spectra.

The first one is the librational motion of amplitude  $\langle \theta \rangle$  around the molecular c.m. (with normal isotopic frequency shift). In a simple harmonic torsional model, the strength of a SM-librational combination band is expected to be  $(dp/dr)_{r_0}^2 \langle \theta \rangle^2$ . Our observed  $\text{OH}^-/\text{OD}^-$  strength ratio of  $\sim 14$  is not easy to divide into the two terms of this product. Assuming for  $\langle \theta \rangle^2$  a ratio of 2, leaves for  $(dp/dr)_{r_0}^2$ , a ratio of  $\sim 7$ , within a factor of two close to the value determined for  $\text{OH}^-/\text{OD}^-$  in KBr. This indicates validity of our above-discussed selected scheme, which does not allow any large isotopic variation of  $(dp/dr)_{r_0}^2$ .

Even more significant are the observed SM phonon combination bands that show two important features:

(a) Their  $\text{OH}^-/\text{OD}^-$  strength ratio of  $\sim 2.5$  is the same as observed in other hosts like KBr and RbCl.

(b) The strengths per 1000 ppm molecules are about two orders of magnitude higher in NaCl, compared to KBr and RbCl hosts.

In an anharmonic lattice vibrational model, the strength of the SM phonon combination band is expected to depend on  $(dp/dr)_{r_0}^2$ , the spectral density of the coupled phonons, and the anharmonic coupling strength between molecular defects and coupled phonons.<sup>30</sup> Among these parameters, only the first one could be strongly changed by the  $\text{OH}^-$  and  $\text{OD}^-$  isotopic substitution. The result (a) however is quite “normal,” because the SM absorption strength is approximately 2–5 times weaker for  $\text{OD}^-$  than for  $\text{OH}^-$  in the above-mentioned host systems. This is within the anharmonic coupling model the convincing evidence for no large variation of  $(dp/dr)_{r_0}^2$  under isotope exchange in NaCl. The other parameters (the spectral density and anharmonic coupling strength of the coupled phonons), however, can depend very much on the host lattice. The result (b) can be attributed to a strong anharmonic coupling of  $\text{OH}^-$  and  $\text{OD}^-$  in NaCl to phonons that are essentially polarized // to the molecular axis or SM (see Fig. 11). Their spectral shape does not follow that of the theoretical phonon-density curve, indicating that they represent selected, more localized modes. Particularly the first peak at  $\sim 100 \text{ cm}^{-1}$  could be due to modes in which a stretching motion of the Na-O distance participates and should couple very strongly to the  $\text{OH}^-$  and  $\text{OD}^-$  stretching mode.

For the SM-librational combination band, a phonon sideband at about the same frequency of  $\sim 80 \text{ cm}^{-1}$  is observed again in // polarization. It could be (somewhat modified in frequency) the same type of modes (as discussed above), which couple not only to the SM, but also to the libration of the molecule. At least for  $\text{OD}^-$ , this phonon sideband is even stronger than the SM-librational combination band.

In summary: Despite the undetectable SM+motional absorption strength of  $\text{OD}^-$  in NaCl, we can conclude that its  $(dp/dr)_{r_0}^2$  is rather “normal” and comparable to that in other hosts like RbCl and KBr. We achieved this result by comparing the relative strength of various combination bands. However, the mysterious weakness of two  $\text{OD}^-$  ab-

sorption transitions (the direct motional and the SM + motional ones) is not yet understood.

## VI. SUMMARY AND FUTURE STUDIES

We have performed low-temperature FTIR and polarized Raman studies of the motional (and librational) transitions of  $^{16}\text{OH}^-$ ,  $^{18}\text{OH}^-$ ,  $^{16}\text{OD}^-$ , and  $^{18}\text{OD}^-$  in NaCl. We observed both direct motional transitions ( $v_0 \rightarrow v_0$ ) and transitions in combination with the stretch mode excitation ( $v_0 \rightarrow v_1$ ). The  $^{16}\text{O} \rightarrow ^{18}\text{O}$  isotope substitution has no detectable effect on the motional states, but  $\text{H} \rightarrow \text{D}$  substitution and  $v_0 \rightarrow v_1$  excitation produce important changes.

From these spectral results, we can construct an energy-level diagram for each of the isotopes and for both vibrational states. We analyzed these by fitting them to a simple  $V_4$  Devonshire model, which describes the motion of off-center molecular defects. The best results were achieved by assuming that the rotational constant (or moment of inertia) is constant, while there is a strong systematic decrease of the potential ( $V_4$  or mixed  $V_4/V_6$ ) along the sequence of systems  $v_0(\text{OH}^-) \rightarrow v_1(\text{OH}^-) \rightarrow v_0(\text{OD}^-) \rightarrow v_1(\text{OD}^-)$ . This describes a change from weakly hindered to quasi-free rotation.

Phenomenological models can describe each individual isotope and SM state fairly well, with a suitable choice of the parameters. Much more important (and still unavailable) would be a model based on the microscopic interactions. Such a model could be used to calculate the off-center potential and physically explain the observed strong variation under  $\text{OH}^- \rightarrow \text{OD}^-$  and  $v_0 \rightarrow v_1$  changes.

Another open question is the nondetectable, small motional absorption of the  $\text{OD}^-$ . Both direct transitions and transitions in combination with the SM are invisible, in contrast with the well-detectable absorptions of the phonon and the librational SM sidebands, and the clearly visible transitions of the  $\text{OH}^-$ . Therefore, we assume that this effect is due to some unknown property of the motional states, and not to an extremely small  $(dp/dr)_{r_0}^2$  of the SM vibration. This could be experimentally verified by studying the SM absorption of the  $\text{OD}^-$  in an environment without symmetry. The symmetry could be removed by interactions with other defects, electromagnetic fields, or elastic stress; in absence of equivalent sites and orientations, we expect a single-line classical SM transition. In this paper, we have tentatively identified the  $B$  band in the middle of the multiline SM absorption spectrum of  $\text{OH}^-$  as an example of this. For  $\text{OD}^-$ , this line has not yet been identified, but we observe [see Fig. 4(a)] many lines of this type, from which one could well be the weak classical SM transition of an isolated fixed  $\text{OD}^-$  defect (and not from pairs or clusters).

An FTIR and Raman study of this system at higher temperatures could also be informative. Because the potential is so weak, the high-temperature spectra look very much like those of a free rotor. It is yet unknown whether the system preserves its off-centerness and rotational constant up to and above room temperature, and whether the motional states change.

## ACKNOWLEDGMENTS

This work was supported by NSF Grant No. DMR 9632959. Support by the FWO (Flemish Fund for Scientific

Research), the IIKW (Interuniversity Institute for Nuclear Sciences), and the Belgian IIKW (Interuniversitary Institute for Nuclear Sciences), and the Belgian Lotto is gratefully acknowledged. E.G. would like to thank the FWO for financial support.

- 
- <sup>1</sup>For an earlier review, see F. Bridges, *Crit. Rev. Solid State Mater. Sci.* **5**, 1 (1975).
- <sup>2</sup>H. B. Shore, *Phys. Rev.* **151**, 570 (1966).
- <sup>3</sup>R. Pirc and P. Gosar, *Phys. Kondens. Mater.* **9**, 377 (1969).
- <sup>4</sup>H. B. Shore and L. M. Sander, *Phys. Rev. B* **6**, 1551 (1972).
- <sup>5</sup>S. Kapphan and F. Luty, *J. Phys. Chem. Solids* **34**, 969 (1973).
- <sup>6</sup>H. Härtel, *Phys. Status Solidi* **42**, 369 (1970).
- <sup>7</sup>For an early review, see F. Luty, *J. Phys. (Paris), Colloq.* **34**, C9-49 (1973).
- <sup>8</sup>S. Kapphan, *J. Phys. Chem. Solids* **35**, 621 (1974).
- <sup>9</sup>C. P. An and F. Luty, *Phys. Rev. B* **56**, R5721 (1997).
- <sup>10</sup>E. Gustin, A. Bouwen, D. Schoemaker, C. P. An, and F. Luty, *Phys. Rev. B* **61**, 3989 (2000).
- <sup>11</sup>M. V. Klein, S. O. Kennedy, T. I. Gie, and B. Wedding, *Mater. Res. Bull.* **3**, 667 (1968).
- <sup>12</sup>H. Fleurent, W. Joosen, and D. Schoemaker, *Phys. Rev. B* **38**, 6257 (1988).
- <sup>13</sup>J. G. Peascoe and M. V. Klein, *J. Chem. Phys.* **59**, 2394 (1973).
- <sup>14</sup>R. D. Kirby, A. E. Hughes, and A. J. Sievers, *Phys. Rev. B* **2**, 481 (1970).
- <sup>15</sup>R. L. Rosenbaum, C-K. Chau, and M. V. Klein, *Phys. Rev.* **186**, 852 (1969).
- <sup>16</sup>R. Windheim and H. Kinder, *Phys. Rev.* **51**, 475 (1975).
- <sup>17</sup>A. F. Devonshire, *Proc. R. Soc. London, Ser. A* **153**, 601 (1936).
- <sup>18</sup>B. Wedding and M. V. Klein, *Phys. Rev.* **177**, 1274 (1969).
- <sup>19</sup>J. F. Zhou, E. Goovaerts, and D. Schoemaker, *Phys. Rev. B* **29**, 5509 (1984).
- <sup>20</sup>S. Suto and M. Ikezawa, *J. Phys. Soc. Jpn.* **53**, 438 (1984).
- <sup>21</sup>T. Nanba, K. Hirota, S. Suto, and M. Ikezawa, *J. Phys. Soc. Jpn.* **53**, 449 (1984).
- <sup>22</sup>H. U. Beyeler, *Phys. Status Solidi B* **52**, 419 (1972).
- <sup>23</sup>C. R. A. Catlow, K. M. Diller, M. J. Norgett, J. Corish, B. M. C. Parker, and P. W. M. Jacobs, *Phys. Rev. B* **18**, 2739 (1978).
- <sup>24</sup>L. V. Gurvich, G. A. Bergman, L. N. Gorokhov, V. S. Iorish, V. Ya. Leonidov, and V. S. Yungman, *J. Phys. Chem. Ref. Data* **25**, 1211 (1996).
- <sup>25</sup>G. Ruanio and S. Rolandson, *Phys. Rev. B* **2**, 2098 (1970).
- <sup>26</sup>D. L. Harrison, Ph.D. thesis, University of Utah, 1970.
- <sup>27</sup>W. Heinicke and F. Luty, *Bull. Am. Phys. Soc.* **17**, 143 (1972).
- <sup>28</sup>R. Callender and S. Pershan, *Phys. Rev. A* **2**, 672 (1970).
- <sup>29</sup>J. G. Peascoe, W. R. Fenner, and M. V. Klein, *J. Chem. Phys.* **60**, 4208 (1974).
- <sup>30</sup>H. Bilz, D. Strauch, and B. Fritz, *J. Phys. (Paris), Colloq.* **27**, C2-3 (1966).